HAL open science

Application of immersed boundary based turbulence wall modeling to the Ahmed body aerodynamics

Shang-Gui Cai, Sajad Mozaffari, Jérôme Jacob, Pierre Sagaut

To cite this version:

Shang-Gui Cai, Sajad Mozaffari, Jérôme Jacob, Pierre Sagaut. Application of immersed boundary based turbulence wall modeling to the Ahmed body aerodynamics. Physics of Fluids, 2022, 34 (9), pp.095106. 10.1063/5.0098232 . hal-04065468

HAL Id: hal-04065468

https://amu.hal.science/hal-04065468v1

Submitted on 11 Apr 2023

HAL is a multi-disciplinary open access archive for the deposit and dissemination of scientific research documents, whether they are published or not. The documents may come from teaching and research institutions in France or abroad, or from public or private research centers.

L'archive ouverte pluridisciplinaire **HAL**, est destinée au dépôt et à la diffusion de documents scientifiques de niveau recherche, publiés ou non, émanant des établissements d'enseignement et de recherche français ou étrangers, des laboratoires publics ou privés.

Application of immersed boundary based turbulence wall modeling to the Ahmed body aerodynamics

Shang-Gui Cai (蔡尚炅), Sajad Mozaffari,[a)] Jérôme Jacob, and Pierre Sagaut

AFFILIATIONS

Aix Marseille Univ, CNRS, Centrale Marseille, M2P2 UMR 7340, Marseille 13451, France

[a)]Author to whom correspondence should be addressed: sajad.mozaffari@univ-amu.fr

ABSTRACT

This paper applies a recently developed immersed boundary-turbulence wall modeling approach to turbulent flows over a generic car geometry, known as the Ahmed body, under massive flow separation within a lattice Boltzmann solver. Although the immersed boundary method combined with hierarchical Cartesian grid offers high flexibility in automatic grid generation around complex geometries, the near-wall solution is significantly deteriorated compared to the body-fitted simulation, especially when coupled to wall models for turbulent flows at high Reynolds number. Enhanced wall treatments have been proposed in the literature and validated for attached flow configurations. In this work, the Ahmed body with a slant surface of angle 35° is considered where the flow separates massively over the slant surface and the vertical base. The large eddy simulation is performed with a Reynolds stress constraint near-wall. The eddy viscosity is computed dynamically by taking into account the actually resolved Reynolds stresses. It approaches the mixing length eddy viscosity in attached boundary layers and returns to the subgrid eddy viscosity in detached boundary layers. An explicit equilibrium wall model has also been proposed to accelerate the calculation. Comparison with the no-slip boundary condition on the separated surfaces shows that the near-wall treatments with the equilibrium wall model operate reasonably well on both attached and detached boundary layers.

I. INTRODUCTION

Aerodynamics are major concerns in automotive designs, as they are directly related to safety, comfort, and fuel consumption. The external flows over ground vehicles are in general highly unsteady, three-dimensional, and often associated with complex turbulent coherent structures. In 1984, Ahmed *et al.*[1] carried out an experimental study on a simplified car geometry with rounded edges at the front and a slanted surface at the rear, later known generically as the Ahmed body. The flow over the Ahmed body reproduces the basic aerodynamic features of ground vehicles, such as the large recirculation zone after the body and complex vortex interactions over the slant surface. It has been shown that the drag is mainly due to the pressure drag, which is strongly affected by the wake behind the body characterized by a separation region and counter-rotating vortices emitted from the slant side edges. The maximum drag is observed at the slant angle of 30°. Above this critical angle, the drag experiences an abrupt decrease, that is the drag crisis, because of the fully detached flow over the slant surface. Virtual wind tunnels using modern computational fluid dynamics can provide more detailed spatial and temporal flow information compared to experimental measurements. However, high fidelity numerical algorithms and turbulence modeling strategies are required to correctly capture the flow topology and the drag production.

The turbulent motions surrounding the ground vehicles span a wide range of scales such that resolving all eddy scales using direct numerical simulation (DNS) is not feasible even with the most advanced computers in the foreseeable future. The statistical modeling of the Reynolds-averaged Navier–Stokes (RANS) remains principally used in the automotive industry. However, it is not reliable for obtaining the flow unsteadiness, especially in the case of massive flow separation. The large eddy simulation (LES), which resolves eddies of size larger than the computational grid and approximates the smaller eddies with subgrid models, has been extensively employed in the virtual wind tunnel. As the eddy size gets progressively smaller toward the wall, resolving the near-wall turbulence at high Reynolds number with LES would be impracticable because it leads to prohibitive grid numbers to the limit of DNS in the near-wall region. Hybrid RANS-LES turbulence models or wall-modeled LES (WMLES), which uses

RANS turbulence models or wall models near the wall to relax the grid requirement, has proven to be an efficient routine for modeling turbulence surrounding vehicles at high Reynolds numbers.

Han[2] conducted earlier numerical studies over the Ahmed body using the $k-\epsilon$ turbulence model with standard wall functions and pointed out the influence of the turbulence model and the numerical schemes to the overall results. Menter and Kuntz[3] also carried out simulations with the $k-\epsilon$ model and the $k-\omega$ shear stress transport (SST) model along with wall models. Although fully separated flows are obtained for the 35° slant angle, the flow topology for the 25° slant angle is much more sensitive to the numerical schemes and the turbulence models, either fully detached or fully separated. They improved the results with the detached eddy simulation (DES) turbulence model and obtained the partial reattachment for the 25° slant angle. Krajnovic and Davidson,[4] followed by Lehmkuhl *et al.*,[5] employed the wall-resolved LES at a smaller Reynolds number for the slant angle of 25° and obtained a good flow topology with accurate turbulence details. They also reported small separations at the leading edge of the front. Fares[6] performed a very large eddy simulation with the lattice Boltzmann method. A volumetric formulation was employed at the boundary to conserve mass and momentum, and a non-equilibrium wall model was used near-wall. Satisfactory results have been obtained for both slant angles, whereas the reattachment is delayed at 25°. The grid resolution was found crucial to the flow separation in Ref. 6. Serre *et al.*[7] presented a comparative analysis for the slant angle 25° with various turbulence models, ranging from wall-modeled and wall-resolved LES to DES, and different discretization methods, including finite-volume method and pseudo-spectral method. Only the pseudo-spectral based LES captured the reattachment over the slant. Guilmineau *et al.*[8] compared the RANS simulations [$k-\omega$ SST model and EARSM (explicit algebraic Reynolds stress model) model] and the hybrid RANS-LES simulations [DES and IDDES (improved delayed DES)], on a highly refined grid in the wall-normal direction. For the slant angle of 35°, all the turbulence models were able to predict the massive flow separation, while the hybrid RANS-LES models predicted a small separation near the slant end which has been confirmed recently by Liu *et al.*[9] For the slant angle of 25°, the partial reattachment over the slant surface was only obtained with IDDES model. Other advanced turbulence models have also been assessed for the Ahmed body aerodynamics, such as the partially averaged Navier–Stokes,[10] the embedded LES,[11] the scale-adaptive simulation, and the stress-blended eddy simulation.[12]

The realistic car geometries are generally complex such that the generation of suitable body-fitted grids is quite cumbersome and time-consuming, even for this simplified body geometry. Using the immersed boundary method (IBM) on Cartesian grids for complex boundaries became more and more popular over the past few decades, see Refs. 13–19, due to the merit of automatic grid generation of high quality. The IBM introduces a source force field or reconstructs the near-wall flow velocity with a prescribed profile to account for the presence of the car body such that the computational grid is not required to conform to the car geometry. By coupling to the turbulence wall models, it can be extended to high Reynolds number wall-bounded turbulent flows. However, spurious oscillations have been frequently observed toward the surface quantities, such as the wall pressure and the skin friction. More severely, the mean level of the skin friction is significantly over-estimated, see Ref. 18. The oscillation stems from the non-constant wall distance of the near-wall grids with the highly nonlinear velocity profile, which renders the near-wall treatments very sensitive to the velocity interpolation and the gradient calculation. The velocity profile is artificially linearized in Refs. 17, 20, and 21 to reduce the steep velocity gradient near-wall. Retrieving the boundary points away from walls is also useful to reduce the oscillations, such as Ref. 19. It is found in Ref. 18 that when the friction velocity is used for interpolation and the gradients are carefully computed, smooth wall surface quantities can be obtained with the nonlinear velocity profile. Nevertheless, most studies of the immersed boundary-turbulence wall model are concentrated on RANS. The extension to LES has been continuously growing, such as Refs. 22 and 23. The crucial aspect is to maintain the total Reynolds stresses in LES between the modeled stress and the resolved stress near-wall for the attached boundary layers.

The present work will extend the immersed boundary-based turbulence wall modeling of Ref. 23 to the aerodynamic predictions of the Ahmed body under massive flow separation via a lattice Boltzmann solver. The paper is organized as follows. The numerical models are described in detail in Sec. II. In the following Sec. III, the computational setup for the Ahmed body case is presented. In Sec. IV, the numerical results are compared to the experimental data and the influences of different near-wall treatments are discussed. Finally, conclusions are offered in Sec. V.

II. NUMERICAL METHODS

A. Lattice Boltzmann based turbulence modeling

The flow solver ProLB is used in the current work with the D3Q19 lattice Boltzmann method (LBM), which has been extensively validated for various turbulent flows, see Refs. 17–19, 23, and 24. The discrete velocity Boltzmann equation is described as follows:

$$\frac{\partial f_\alpha}{\partial t} + \mathbf{c}_\alpha \cdot \nabla f_\alpha = \mathbf{\Omega}_\alpha, \tag{1}$$

where f_α represents the particle distribution function spanned in the velocity space of the α-th direction. $\mathbf{c}_\alpha$ is the discrete velocity vector, and $\mathbf{\Omega}_\alpha$ signifies the particle collision operator. Integrating over the characteristic line and adopting the Bhatnagar–Gross–Krook (BGK) collision model give to the following lattice Boltzmann equation:

$$f_\alpha(\mathbf{x} + \mathbf{c}_\alpha \Delta t, t + \Delta t) - f_\alpha(\mathbf{x}, t) = -\frac{\Delta t}{\tau}\left(f_\alpha(\mathbf{x}, t) - f_\alpha^{\mathrm{eq}}(\mathbf{x}, t)\right), \tag{2}$$

where the particle distribution function is relaxed toward an equilibrium state after collision within a relaxation time τ. f_α^{eq} represents the equilibrium function truncated from the Maxwell-Boltzmann distribution (see Ref. 24). By taking the moments of the particle distribution function, one can obtain successively the density,

$$\rho = \sum_\alpha f_\alpha(\mathbf{x}, t), \tag{3}$$

and the momentum flux,

$$\rho \mathbf{u} = \sum_\alpha \mathbf{c}_\alpha f_\alpha(\mathbf{x}, t). \tag{4}$$

The total viscosity is related to the relaxation time by

$$\nu_{\text{tot}} = c_s^2\left(\tau - \frac{\Delta t}{2}\right), \tag{5}$$

where c_s is the lattice sound speed. For the D3Q19 model, $c_s = 1/\sqrt{3}$. The pressure can be recovered by

$$p = \rho c_s^2. \tag{6}$$

It can be demonstrated that the weakly compressible athermal Navier–Stokes equations ($Ma < 0.3$) can be derived from the lattice Boltzmann equation through the Chapman–Enskog expansion. The LBM is very advantageous compared to the Navier–Stokes based solvers for the following reasons. First, the time advancement is realized explicitly by simple collision and streaming processes. Second, LBM is highly suitable for parallel computing, since the collision step is a local operation and the streaming step is nothing but swift in memory address of the particle distribution functions.

Nevertheless, the BGK collision model is not stable at high Reynolds number as it is not able to remove spurious energy generated during the calculation. For stabilization, the density-based hybrid recursive regularized model (HRR-ρ) is developed in Jacob *et al.*,[24] which expands the non-equilibrium part of the particle distribution function $f_\alpha^{(1)}$ into Hermite series and introduces a hyper viscosity to the collision as

$$\Omega_\alpha = -\frac{1}{\tau}\left(f_\alpha^{(1)}\sigma - (1-\sigma)\frac{\rho\tau}{c_s^2}\mathscr{H}_\alpha^{(2)} : \mathbf{S}^{\text{FD}}\right), \tag{7}$$

where $\mathscr{H}_\alpha^{(2)} = \mathbf{c}_\alpha\mathbf{c}_\alpha - c_s^2\mathbf{I}$ denotes the second order Hermite tensor and $\mathbf{I}$ is the identity matrix. $\mathbf{S}^{\text{FD}}$ represents the strain rate tensor that is evaluated using finite difference. The amount of hyper viscosity for stabilization is controlled by the value of σ, which is chosen as close to unity as possible.

The Favre filtered Navier–Stokes equations resulting from the HRR-ρ LBM can be written as

$$\frac{\partial\bar{\rho}}{\partial t} + \frac{\partial\bar{\rho}\tilde{u}_i}{\partial x_i} = 0, \tag{8}$$

$$\frac{\partial\bar{\rho}\tilde{u}_i}{\partial t} + \frac{\partial}{\partial x_j}(\bar{\rho}\tilde{u}_i\tilde{u}_j) = -\frac{\partial\bar{p}}{\partial x_i} + \frac{\partial\tilde{\sigma}_{ij}}{\partial x_j} - \frac{\partial\tau_{ij}}{\partial x_j} + E - G\left(\sigma, \Delta^2, \frac{\partial^4\tilde{u}_i}{\partial x_j^4}\right), \tag{9}$$

where E is the high order term that can be negligible at low Mach number flows. The last term G arises from the hyper viscosity that depends on the σ value, the grid size Δ, and the fourth-order derivative of the velocity. The viscous stress tensor $\tilde{\sigma}_{ij}$ is given by

$$\tilde{\sigma}_{ij} = 2\bar{\rho}\nu\left(\tilde{S}_{ij} - \frac{1}{3}\tilde{S}_{kk}\delta_{ij}\right), \quad \tilde{S}_{ij} = \frac{1}{2}\left(\frac{\partial\tilde{u}_i}{\partial x_j} + \frac{\partial\tilde{u}_j}{\partial x_i}\right), \tag{10}$$

where ν is the molecular viscosity and δ_{ij} represents the Kronecker delta function. Under the eddy viscosity assumption, the subgrid stress tensor τ_{ij} can be expressed as

$$\tau_{ij} = -2\bar{\rho}\nu_t\left(\tilde{S}_{ij} - \frac{1}{3}\tilde{S}_{kk}\delta_{ij}\right) + \frac{1}{3}\tau_{kk}\delta_{ij}. \tag{11}$$

For the Vreman's subgrid model,[25] the eddy viscosity is given by

$$\nu_t = 2.5C_s^2\Delta^2\sqrt{\frac{B_\beta}{A_\beta}}, \tag{12}$$

where $C_s \approx 0.1$ is the Smagorinsky constant and Δ is the filter size, which is taken as the grid size. A_β and B_β are the first and the second invariants of the tensor $\boldsymbol{\beta}$ given by

$$\boldsymbol{\beta} = \boldsymbol{\alpha}^{\text{T}} \cdot \boldsymbol{\alpha} = \alpha_{ki}\alpha_{kj}, \quad \alpha_{ij} = \frac{\partial\tilde{u}_j}{\partial x_i} \tag{13}$$

and

$$A_\beta = \text{tr}(\boldsymbol{\beta}) = ||\boldsymbol{\alpha}||^2 = \alpha_{ij}\alpha_{ij}, \tag{14}$$

$$\begin{aligned} B_\beta &= \frac{1}{2}\left[(\text{tr}(\boldsymbol{\beta}))^2 - \text{tr}(\boldsymbol{\beta}^2)\right] \\ &= \beta_{11}\beta_{22} - \beta_{12}^2 + \beta_{11}\beta_{33} - \beta_{13}^2 + \beta_{22}\beta_{33} - \beta_{23}^2. \end{aligned} \tag{15}$$

Finally, by summing up the molecular viscosity and the eddy viscosity, the total viscosity is transformed into the relaxation time through Eq. (5) to be accounted in the LBM simulations.

B. General boundary conditions for LBM

1. *Immersed boundary condition*

Since LBM principally works on Cartesian grids, it is inherently a non-body fitting grid method for general boundaries. Even though the bounce-back scheme can be applied to complex geometries, it is confined to no-slip wall boundaries. Other types of boundary conditions like inflow, outflow, and frictionless wall on curved boundaries are more difficult to constructed heuristically from the particle distribution functions.

The IBM facilitates the implementation of boundary conditions for LBM. Figure 1(a) illustrates the definition of the immersed boundary conditions on the off-surface grid points, referred to boundary points. Several fictitious reference points are established along the wall-normal direction passing the boundary points at a distance of the local grid size successively, and their values are interpolated from the neighbor points. Therefore, linear or quadratic profiles can be constructed for the generic quantity q (e.g., velocity or density) using Lagrange polynomial. For Dirichlet boundary conditions (e.g., inflow velocity, or no-slip velocity), the boundary value away from the physical surface at a normal distance d can be interpolated along the wall-normal line quadratically,

$$q_b = -\frac{-2q_s + dq_2 + d^2q_2 - 2d^2q_1 - 4dq_1}{(d+2\Delta)(d+\Delta)}, \tag{16}$$

or linearly,

$$q_b = \frac{\Delta q_s + dq_1}{d+\Delta}, \tag{17}$$

where q_1 and q_2 indicate values at the two reference points and q_s represents the surface value. For Neumann boundary conditions (e.g., outflow velocity), the boundary value can be determined using a quadratic profile

$$q_b = \frac{4q_1 - q_2}{3\Delta}, \tag{18}$$

or using a linear profile

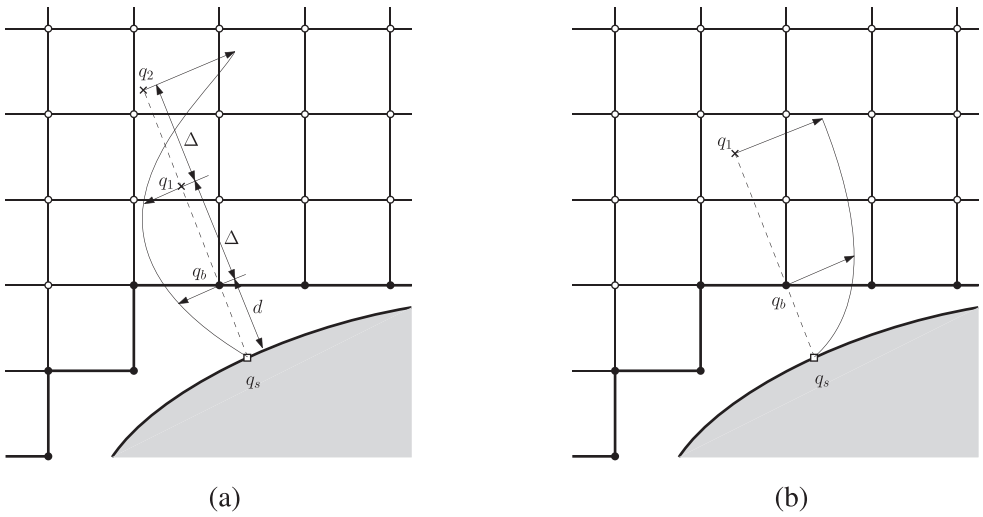

FIG. 1. Schematic of the immersed boundary condition: (a) general boundary condition and (b) wall-law boundary condition. Boundary points (solid circles), fluid points (empty circles), reference points (cross), and physical surface points (empty squares).

$$q_b = q_1, \tag{19}$$

where the zero gradient condition is assumed at the boundary points.

As a matter of fact, the evolutionary variables for LBM are the particle distribution functions. Therefore, there is a need to transform the macroscopic boundary conditions to the particle distribution functions. In HRR-ρ LBM, all the particle distribution functions are reconstructed by the sum of the equilibrium part and the non-equilibrium part

$$f_\alpha = f_\alpha^{\mathrm{eq}}(\rho, \mathbf{u}) + f_\alpha^{(1)}(\nu_{\mathrm{tot}}, \mathbf{S}^{\mathrm{FD}}), \tag{20}$$

where the strain rate is computed by finite difference at boundary points.

2. Sponge layer

To prevent outer boundary spurious reflections from deteriorating interior flow fields, a sponge or damping region is defined close to the domain boundary as a source penalty term

$$-\lambda\sigma_s(d)(q - q_{\mathrm{ref}}), \tag{21}$$

where λ is the sponge strength. The time-averaged value is used for the target or reference value, $q_{\mathrm{ref}} = \bar{q}$, which is computed recursively using the exponentially weighted moving average[26] as follows:

$$\bar{q}^{n+1} = (1 - C_{\exp})\bar{q}^n + C_{\exp} q^{n+1}, \tag{22}$$

where $n+1$ represents current time level and $\bar{q}^0 = q^0$. This average effectively extracts the low-frequency component of the flow field, with $C_{\exp}$ related to the cutoff frequency f_c by $C_{\exp} = 3.628 f_c \Delta t$. The exponentially weighted moving average keeps all the time histories but gives more influences to recent values. The damping function described in Ref. 27 is employed in the present work:

$$\sigma_s(d) = \frac{3125}{256}\frac{d(L_s - d)^4}{L_s^5}, \tag{23}$$

where L_s represents the thickness of the sponge layer.

C. Immersed boundary-turbulence wall modeling

1. Attached boundary layer

For attached turbulent boundary layers under zero pressure gradient, there exists the law of the wall in the inner part where distinct layers can be identified, namely, the viscous sublayer, the buffer layer, and the inertial layer. Although non-equilibrium effects, such as the unsteadiness, the pressure gradient, or the convection, can be added for more physics, a proper implementation is still arguable, see Ref. 28. Hence, throughout this paper, only the equilibrium wall model is considered. The wall model can be used to specify the wall shear stress boundary condition for LES, that is, the wall-modeled LES. This significantly reduces the computational demand by the no-slip boundary condition where extra fine grids are required, to the limit of DNS, in both wall-parallel and wall-normal directions for LES to resolve the near-wall turbulent motions. The traditional logarithmic wall model, however, relies on the Newton's iteration to determine the friction velocity u_τ, given the wall-tangential velocity u, and the wall-normal distance y. The newly explicit wall model is proposed in Refs. 23 and 29 to eliminate unnecessary iterations and to enhance the computational stability, which is summarized as follows:

$$y^+(Re_y) = \left[1 - \tanh\left(\frac{Re_y}{180.8}\right)\right]^{0.789}(Re_y)^{1/2} + \left[\tanh\left(\frac{Re_y}{180.8}\right)\right]^{0.789}\frac{1}{E}e^{W(\kappa E Re_y)}, \tag{24}$$

where the local Reynolds number is defined as $Re_y = uy/\nu$ and, hence, the friction velocity is computed explicitly by $u_\tau = y^+(Re_y)\nu/y$. The Lambert W function in Eq. (24) is given by

$$W(\kappa E Re_y) = \log\left(\frac{\kappa E Re_y}{W(\kappa E Re_y)}\right), \tag{25}$$

which is expanded explicitly into series to avoid the Newton's iteration.[23,29]

Figure 1(b) depicts the immersed boundary based turbulence wall modeling, where the wall distance of the near-wall grids is distributed arbitrarily along the wall surface. It deteriorates significantly the near-wall solution by introducing spurious oscillations to the wall pressure and the skin friction. Smoothing the wall surface quantities has been a continuously growing research topic in recent years, see Refs. 17–21. The root of the spurious oscillations originates from the under-resolved steep velocity gradient over the stair-case boundaries, as discussed previously. Consequently, large errors are introduced during the velocity interpolation and the calculation of the velocity gradient on the boundary points.

To obtain the friction velocity on the boundary points, it is preferable to interpolate the friction velocity instead of the flow velocity from the neighbor points.[18,19] It, thus, needs to invert the wall model at neighbor points, but it does not increase significantly the computation thanks to the explicit wall model. It is found in Cai *et al.*[18] that the surface quantities are greatly smoothed even with a low order interpolation kernel, such as the inverse distance weighting. This is because the friction velocity behaves smoothly among the near-wall grids as opposed to the flow velocity. With the interpolated friction velocity, the tangential velocity on the boundary points can be computed by $u = u_\tau u^+$ with a consistent wall model defined as follows:[23,29]

$$u^+ = \left[1 - \tanh\left(\frac{y^+}{10.71}\right)\right]^{1.526} y^+ + \left[\tanh\left(\frac{y^+}{10.71}\right)\right]^{1.526} \frac{1}{\kappa}\log(Ey^+), \quad E = 11.27. \tag{26}$$

The velocity gradient should be paid attention at the boundary. The weighted least square method usually used for body-fitted grids is employed in the present work. It solves a linear system for the unknown velocity gradients, see Refs. 18, 20, and 21. Moreover, the normal gradient of the tangential velocity is highly underestimated regardless of the accuracy of the gradient schemes. It is reconstructed via a discrete wall-law gradient as suggested in Refs. 18 and 19.

It is known that the immersed boundary method is not conservative over the non-fitted boundary. One prominent issue is that the overall Reynolds stress is not maintained in the wall proximity. As a consequence, the skin friction deviates significantly in both eddy-modeled and eddy-resolved simulations.[18,23] Particularly in LES, the turbulence development is strongly delayed.[23] Therefore, it is necessary to enforce the modeled stress up to several grid points from wall. This is realized dynamically by augmenting the eddy viscosity, also termed as the constrained LES (CLES) in Refs. 30 and 31, with the consideration of the actually resolved turbulent stresses as proposed in Ref. 23,

$$\nu_t^{\text{hybrid}} = \frac{2\nu_t^{\text{RANS}}\langle\tilde{S}_{ij}\rangle\langle\tilde{S}_{ij}\rangle + R_{ij}^{\text{LES}}\langle\tilde{S}_{ij}\rangle}{2\langle\tilde{S}_{ij}\rangle\langle\tilde{S}_{ij}\rangle}, \tag{27}$$

where the mixing length model is employed for $\nu_t^{\text{RANS}}/\nu = \kappa y^+(1 - e^{-y^+/19})^2$ and $R_{ij}^{\text{LES}} = \langle\tilde{u}_i\tilde{u}_j\rangle - \langle\tilde{u}_i\rangle\langle\tilde{u}_j\rangle$ is the resolved Reynolds stress. This hybrid eddy viscosity approaches the RANS eddy viscosity for attached boundary layers and reduces to the LES viscosity for separated boundary layers automatically.

2. Detached boundary layer

As discussed previously, equilibrium or non-equilibrium wall models are basically developed for attached boundary layers, which assumes the quasi-parallel flow near the wall. Therefore, using wall model in the region of flow separation is physically not appropriate. Nevertheless, as a matter of fact, the wall shear stress is rather small in the region of separation such that the wall model would operate in low y^+ ranges where linear profile applies. It has been shown in Refs. 7, 32, and 33 that the flow is not very sensitive to the wall model in the recirculation zone. Moreover, the pressure is nearly constant in the recirculation core.

For the slant angle of 35°, the flow detaches massively from the upstream edge of the slant surface. Hence, the no-slip boundary condition can be specified in advance to the slant surface and the vertical base, while the wall model still applies to the rest of the Ahmed body, including the stilts and the floor.

It is noted that the flow impinges on the front of the body and the flow climbing over the rounded edge might experience significant pressure gradient effect. However, since the flow at these regions are seldom investigated numerically or experimentally in the literature and the drag is largely determined by the wake flow, the equilibrium wall model is adopted at these places in current study. We will demonstrate in Sec. IV that the current wall model is able to handle the attached boundary layer and the detached boundary layer simultaneously without any user intervention.

III. COMPUTATIONAL SETUP

The geometry of the Ahmed body is defined in Fig. 2 for which experimental results are well documented in Refs. 1, 9, and 34. The length, height, and width of the main body are $L = 1.044$ m, $H = 0.288$ m, and $W = 0.389$ m, respectively. The main body is supported by four stilts with a ground clearance of $G = 0.05$ m that are represented by cylinders of diameter 0.03 m. The contribution of the stilts to the drag is non-negligible in the experiments; hence, they are fully considered in the drag evaluation in current work.

The Reynolds number is $Re_H = U_\infty H/\nu = 7.68 \times 10^5$, based on the inflow velocity $U_\infty = 40$ m/s and the body height H, conforming with the experiments conducted by Lienhart and Becker.[34] The flow structures over the Ahmed body are highly three-dimensional and principally determined by the slant angle φ. At small angles

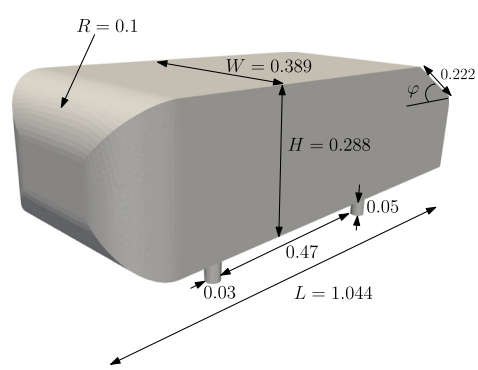

FIG. 2. The geometrical dimension of the Ahmed body (unit [m]), where the slant angle $\varphi = 35°$ is considered in the present work.

TABLE I. Estimation of the non-dimensional turbulent length scales.

λ_H/H	η_H/H	δ/H	δ_ν/H
6.3×10^{-3}	4.6×10^{-5}	6.9×10^{-2}	3.4×10^{-5}

($\varphi < 30°$), three major coherent structures can be identified in the wake, namely, a flow separation and reattachment on the slant surfaces forming a separation bubble, a pair of counter-rotating longitudinal or C-pillar vortices generated from the slant side edges, and two recirculation bubbles after the vertical base. Increasing the slant angle the drag is increased, and the maximum drag is found toward $\varphi = 30°$. Above this critical angle ($\varphi > 30°$), the flow fully detaches from the slant surface due to the strong adverse pressure gradient between the slant and the roof, which finally causes an abrupt drag reduction, i.e., the drag crisis. In this work, we consider the slant angle of $\varphi = 35°$ to assess the proposed method with massive flow separations.

The computational domain is about $8L \times 5W \times 5H$ as defined in the ERCOFTAC benchmark test,[35] where the Ahmed body is placed $2L$ and $5L$ away from the inlet and the outlet, respectively. It implies to a blockage ratio of 4%, whereas the experiments are conducted in a 3/4 open test section. The inlet turbulence intensity in the experiments is reported to be less than 0.25%; hence, it is reasonable to use an uniform inflow condition. The outlet is set to be the ambient pressure. Frictionless boundary conditions are applied for the top boundary and the two sides. The floor and the Ahmed body are modeled with walls. To prevent spurious reflections, the sponge layer is added near the outer boundaries except for the walls.

The turbulent flows involve a large range of length scales. The Taylor scale describing the integral motions in the wake is estimated to $\lambda_H/H \approx 5.5Re_H^{-1/2}$, and the Kolmogorov length scale representing the smallest turbulent scale is about $\eta_H/H \approx 1.2Re_H^{-3/4}$, as estimated in Refs. 6, 8, and 36. The Reynolds number $Re_L = U_\infty L/\nu$ based on the body length can be used to estimate the boundary layer thickness at the rear end $\delta/L \approx 0.37Re_L^{-1/5}$ and the viscous sublayer height $\delta_\nu/L \approx 5.9Re_L^{-0.9}$. These length scales are summarized in Table I. Apparently resolving down to the Kolmogorov scale or even the viscous sublayer is not feasible within current hierarchical grid architecture.

In accordance with these estimations, computational grids are constructed using the Octree grid structure, as displayed in Fig. 3. The coarsest grid spacing used far away from the walls is about $\Delta x_{\max}/H = 0.58$, and the grid is successively refined surrounding the region of interest. For the grid sensitivity study, grids with different levels of refinements are investigated, as given in Table II, where the fine grid is composed of an additional refined wake region. It can be

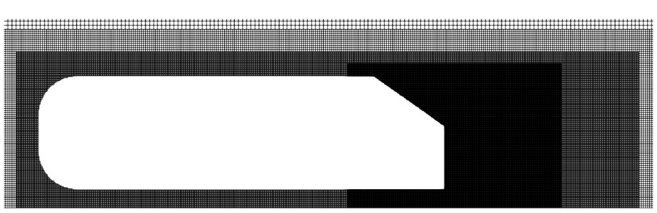

FIG. 3. The computational grid at the y-center plane, shown from the fine grid.

TABLE II. Summary of the spatial and temporal resolutions.

Grid	$\Delta x_{\min}$ [m]	$\Delta x_{\min}/H$	$\Delta x_{\min}/\lambda_H$	Total grid number	$\Delta t_{\min}$ [s]
Coarse	2.6×10^{-3}	9.0×10^{-3}	1.4	1.36×10^7	8.8×10^{-6}
Fine	1.3×10^{-3}	4.5×10^{-3}	0.7	4.03×10^7	4.4×10^{-6}

seen that the Taylor scale is only marginally represented by the fine grid. The time step Δt in LBM is fully determined by the minimal grid size $\Delta x_{\min}$ as follows:

$$\Delta t = \frac{c_s}{c_0}\Delta x_{\min}, \tag{28}$$

where c_0 is the physical sound speed. Hence, the time step is sufficiently small to resolve all temporal scales in LBM. The simulation is lasted over 200 flow-through-time H/U_∞ and averaged for the last 150 flow-through-time. The initial condition is supplied with a previous instantaneous simulation with fully developed turbulent flows. In fact for nearly incompressible flows, the Mach number will not affect significantly the physical results. Therefore, the Mach number is increased artificially from Ma = 0.12 to 0.24 to accelerate the convergence.[6] It is achieved by reducing the physical sound speed c_0, which is meant to increase the time step Δt in view of Eq. (28).

IV. NUMERICAL RESULTS

In this section, the numerical results obtained with the proposed near-wall treatments are compared to the experimental results of Lienhart and Becker.[34] For clarity, we denote "no-slip" for the simulation using the no-slip boundary condition on the slant surface and the vertical base, while the wall-law is still applied to the other parts of the Ahmed body. On the contrary, we refer "wall-law" to the calculation in which the wall model is imposed all over the Ahmed body.

The vortex structures are shown in Fig. 4 by the Q-criterion ($Q = -\frac{1}{2}\frac{\partial \bar{u}_i}{\partial x_j}\frac{\partial \bar{u}_j}{\partial x_i} > 0$). The massive flow separation near the rear end is apparent for all the simulations, and very rich turbulent behaviors are observed in the wake, in spite of the augmentation of the eddy viscosity near-wall. The wall-law boundary condition on the slant surface gives to a small C-pillar vortex, which finally breaks in the wake. However, the onset of flow separation is delayed compared to the case with the no-slip boundary condition on the slant surface. This can be further verified by the streamlines in the wake (Fig. 5) and the friction line on the body surface (Fig. 6). A small separation region can be found near the slant end especially with the no-slip boundary condition, which has been observed numerically and experimentally in Refs. 8 and 9. However, the no-slip boundary condition causes a larger recirculation region in the bottom. The wake can be examined from the iso-contours of the mean streamwise velocity in the successive yz-plane, see Fig. 7. The minimum value of the streamwise velocity indicates the vortex center. The recirculation region extends up to $x = 0.2$ m shown by the negative streamwise velocity, which accords to the experimental observation. The shape of the iso-contours with the wall-law boundary condition is different from those with the no-slip boundary condition, which is due to the existence of the C-pillar vortex.

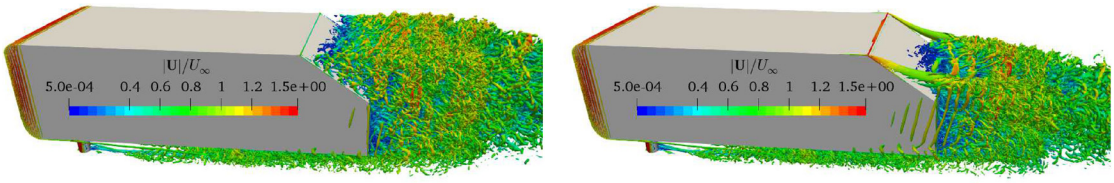

(a) (b)

FIG. 4. Visualization of the vortex structures around the Ahmed body by the *Q*-criterion colored by the velocity magnitude: (a) no-slip and (b) wall-law.

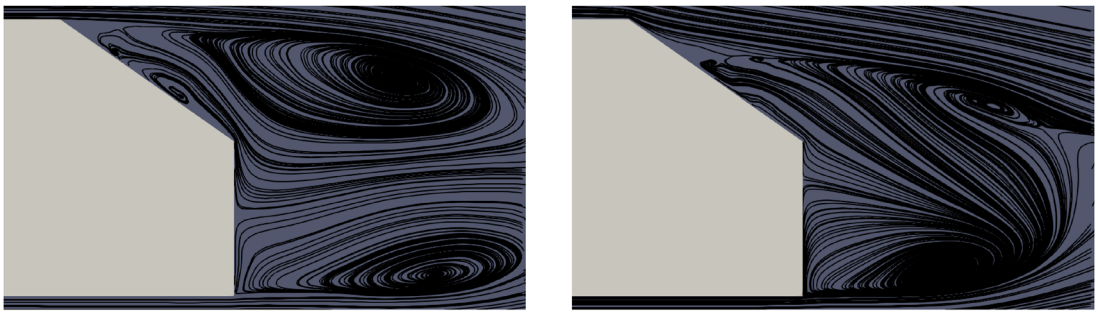

(a) (b)

FIG. 5. Center plane time-averaged streamlines around the rear end of the Ahmed body: (a) no-slip and (b) wall-law.

Figure 8 depicts the first-order and the second-order turbulence statistics of the flow around the Ahmed body, and Fig. 9 gives more comparisons of the flow on the slant surface and provides an enlarged view of the wake. It can be seen that the flows in front and on top of the Ahmed body are well predicted for all the simulations, while the differences become apparent on the slant surface and in the wake.

The grid resolution is very influential for the wall-law boundary condition as the flow does not show any separation over the slant surface on the coarse grid. One reason for the nonphysical attachment is the assumption that the wall shear stress and the tangential velocity at the boundary points are always in the same direction of the near-wall fluid points. Another reason is the lack of enough turbulence stresses to drive the flow separation close to wall. The normal velocity at the boundary points, however, has a negligible effect on the results. Hence, it is simply set to zero in the wall-law setting. By increasing the grid resolution, the flow separates massively from the slant surface and

(a) (b)

FIG. 6. Friction line on the Ahmed body surface on the fine grid: (a) no-slip and (b) wall-law.

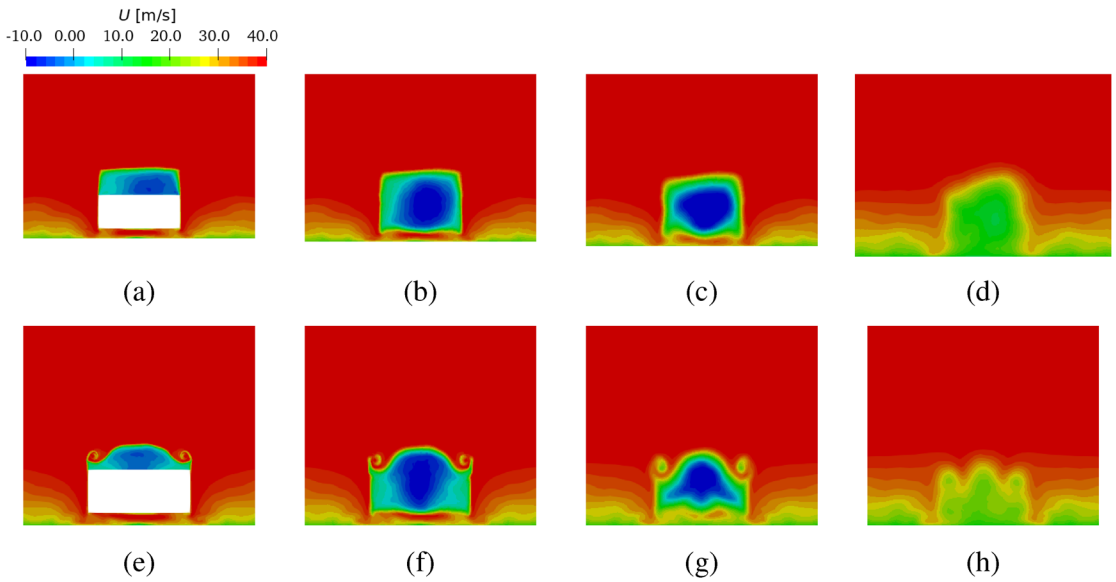

FIG. 7. Iso-contours of the mean streamwise velocity in successive yz-planes in the wake of the Ahmed body: (a)–(d) for no-slip boundary condition and (e)–(h) for wall-law boundary condition. From left to right, the columns correspond to the location $x = 0$, 0.08, 0.2, and 0.5 m, respectively.

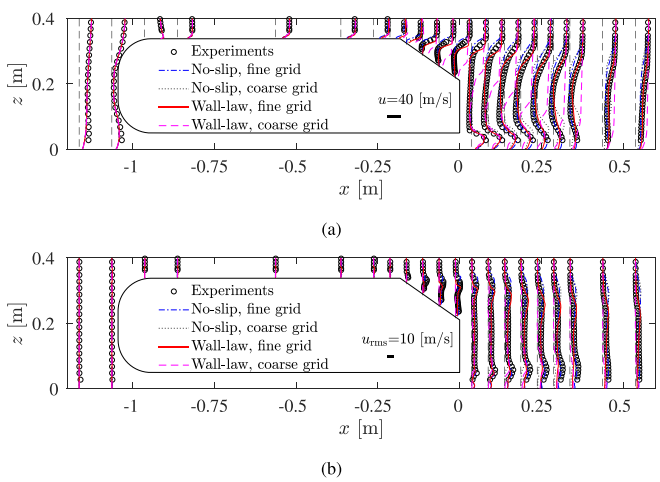

FIG. 8. Comparison of the turbulence statistics for the flow past the Ahmed body. (a) The mean streamwise velocity. (b) The rms of the streamwise velocity.

the resolved turbulent fluctuations are well compared to the experiments toward the end of the slant surface. Enhancing the Reynolds stress close to wall is very essential to drive the flow to separate in the immersed boundary framework. Without this enhancement, the flow stays attached even by refining the grid.

Nevertheless, the no-slip boundary condition leads to flow separation more easily, as illustrated in Fig. 4. It can be found that the no-slip boundary condition on the coarse grid fits quite well to the experimental data on the slant surface but produces unsatisfactory results in the wake near the bottom. On the fine grid, the wake is well calculated by the no-slip boundary condition but it deviates from the experiments on the slant surface due to an early flow separation. Overall on the fine grid, the wall-law boundary condition outperforms the no-slip boundary condition.

Table III summarizes the drag coefficient C_d for the all current simulations and compares to the experimental and other numerical data, where the corresponding Reynolds numbers are converted to Re_H based on the body height H. The drag coefficient is defined by

$$C_d = \frac{F_d}{1/2\rho_\infty U_\infty^2 A}, \tag{29}$$

where $A = W \times H$ is the projected area of the Ahmed body in the streamwise direction. F_d refers to the streamwise drag force, which is obtained either by integrating the surface pressure and the shear stress over the entire Ahmed body including the four stilts (near-field approach) or by integrating over a control volume surrounding the Ahmed body (far-field approach, see Ref. 18). All present results are close to the existing values. In spite of the non-body fitting grid, the predicted drag with current wall modeling on the fine grid is more closer to the experimental results of Meile *et al.*,[37] compared to the body fitting simulations of Guilmineau *et al.*[8] on a highly refined wall-normal grid with IDDES. This can be also attributed to the fact that the current approach is capable to maintain the total Reynolds stress near-wall and can switch the RANS mode and the LES mode for attached and separated boundary layers seamlessly. It should also be noted that the influence of grid resolution on the drag coefficient is larger for the wall-law boundary condition, as the flow exhibits different topology on the coarse and fine grids.

V. CONCLUSION

In this paper, we have extended the immersed boundary-based turbulence wall modeling using a LBM solver for the turbulent flows over the Ahmed body. We have focused on the slant angle of 35°, where the flow separates massively from the slant surface, to study the

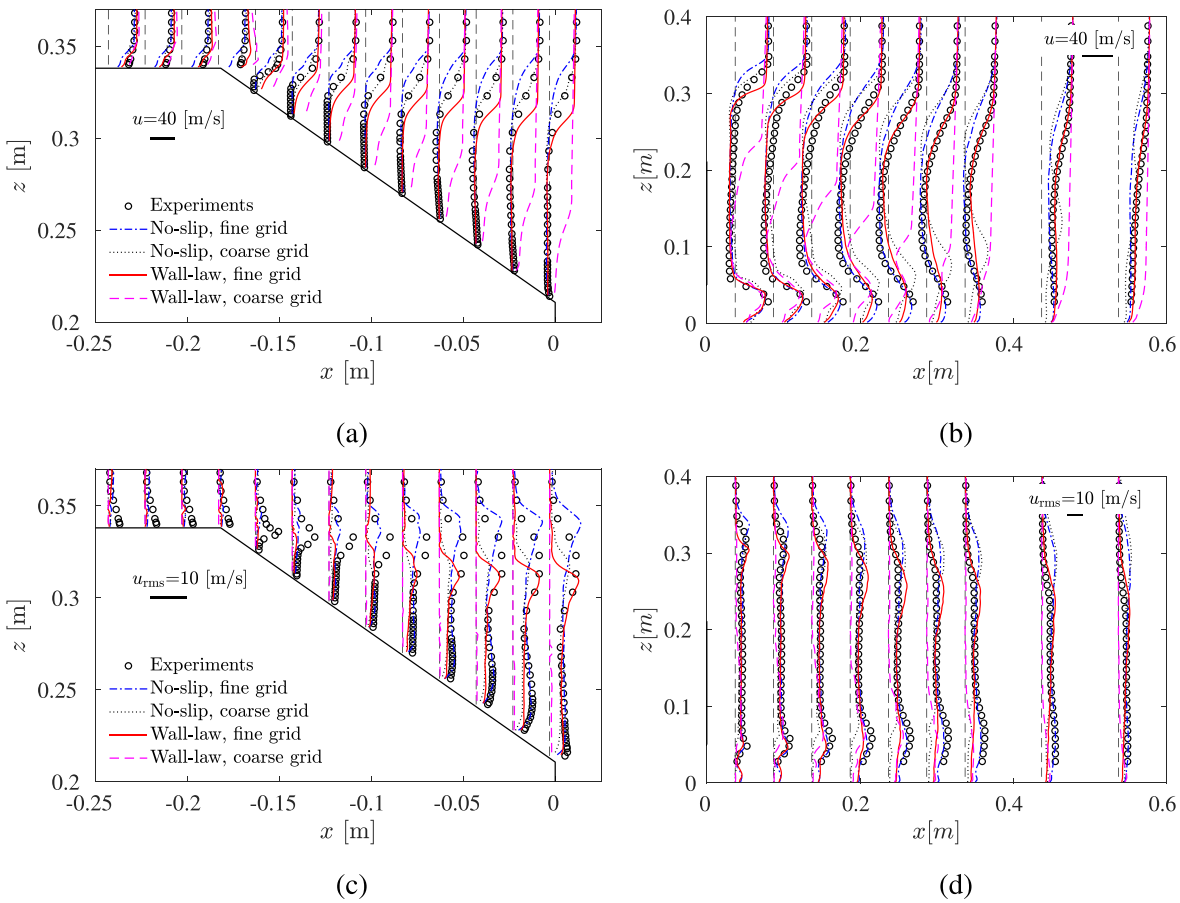

FIG. 9. Comparison of the turbulence statistics on the slant surface and in the wake. The mean streamwise velocity on the slant surface (a) and in the wake (b). The rms of the streamwise velocity on the slant surface (c) and in the wake (d).

TABLE III. Comparison of the drag coefficient for the Ahmed body at the slant angle of 35°, where the no-slip boundary condition is applied to the entire Ahmed body in Ref. 8, but is only imposed on the slant surface in present work. N.A. represents not applicable.

	Method	Boundary condition	Drag evaluation	Re_H	C_d
Ahmed *et al.*[1]	Experiment	N.A.	N.A.	1.2×10^6	0.26
Meile *et al.*[37]	Experiment	N.A.	N.A.	7.68×10^5	0.279
Liu *et al.*[9]	Experiment	N.A.	N.A.	1.4×10^5	0.32
Guilmineau *et al.*[8]	$k-\omega$ SST	No-slip	Near-field	7.68×10^5	0.2999
	EARSM	No-slip	Near-field	7.68×10^5	0.2603
	DES	No-slip	Near-field	7.68×10^5	0.3156
	IDDES	No-slip	Near-field	7.68×10^5	0.3452
Present	CLES	Wall-law, fine grid	Near-field	7.68×10^5	0.2347
			Far-field	7.68×10^5	0.2380
	CLES	Wall-law, coarse grid	Near-field	7.68×10^5	0.2742
			Far-field	7.68×10^5	0.2912
	CLES	No-slip, fine grid	Near-field	7.68×10^5	0.2553
			Far-field	7.68×10^5	0.2588
	CLES	No-slip, coarse grid	Near-field	7.68×10^5	0.2548
			Far-field	7.68×10^5	0.2486

range of applicability of the wall-law boundary condition for attached and detached flow scenarios. For better comparison, we have also considered the no-slip boundary condition on the detached boundaries (the slant surface and the vertical base). The results have shown that the wall-law boundary condition is suitable for both flow regions provided with adequate grid resolution. The slant angle of 25° is still challenging for the wall modeling of flow separation and reattachment, which remains our future work.

ACKNOWLEDGMENTS

The support of the Agence nationale de la recherche (ANR) Industrial Chair ALBUMS (Grant No. ANR-18-CHIN-0003-01) and the Direction générale de l'aviation civile (DGAC) Project No. 2018-16 OMEGA3 are greatly acknowledged. This work was performed using high performance computing resources from Grand équipement national de calcul intensif (GENCI)-Très grand centre de calcul (TGCC) (Grant No. 2021-A0092A07679). Centre de Calcul Intensif d'Aix-Marseille is acknowledged for granting access to its high performance computing resources.

AUTHOR DECLARATIONS

Conflict of Interest

The authors have no conflicts to disclose.

Author Contributions

Shang-Gui Cai: Conceptualization (lead); Data curation (lead); Formal analysis (equal); Investigation (equal); Methodology (lead); Software (lead); Validation (lead); Visualization (lead); Writing – original draft (lead). **Sajad Mozaffari:** Conceptualization (supporting); Data curation (supporting); Investigation (equal); Methodology (supporting); Software (supporting); Writing – original draft (supporting); Writing – review and editing (equal). **Jerome Jacob:** Conceptualization (supporting); Methodology (supporting); Resources (lead); Software (supporting); Supervision (equal); Writing – review and editing (equal). **Pierre Sagaut:** Conceptualization (supporting); Funding acquisition (lead); Methodology (supporting); Supervision (equal); Writing – review and editing (equal).

REFERENCES

[1] S. Ahmed, G. Ramm, and G. Faltin, "Some salient features of the time-averaged ground vehicle wake," SAE Technical Paper No. 840300, 1984.
[2] T. Han, "Computational analysis of three-dimensional turbulent flow around a bluff body in ground proximity," AIAA J. **27**, 1213–1219 (1989).
[3] F. R. Menter and M. Kuntz, "Adaptation of eddy-viscosity turbulence models to unsteady separated flow behind vehicles," in *The Aerodynamics of Heavy Vehicles: Trucks, Buses, and Trains*, edited by R. McCallen, F. Browand, and J. Ross (Springer, Berlin/Heidelberg, 2004), pp. 339–352.
[4] S. Krajnovic and L. Davidson, "Large eddy simulation of the flow around an Ahmed body," in *Proceedings of HT-FED04* (ASME, 2004).
[5] O. Lehmkuhl, G. Houzeaux, H. Owen, G. Chrysokentis, and I. Rodriguez, "A low-dissipation finite element scheme for scale resolving simulations of turbulent flows," J. Comput. Phys. **390**, 51–65 (2019).
[6] E. Fares, "Unsteady flow simulation of the Ahmed reference body using a lattice Boltzmann approach," Comput. Fluids **35**, 940–950 (2006).
[7] E. Serre, M. Minguez, R. Pasquetti, E. Guilmineau, G. B. Deng, M. Kornhaas, M. Schäfer, J. Fröhlich, C. Hinterberger, and W. Rodi, "On simulating the turbulent flow around the Ahmed body: A French-German collaborative evaluation of LES and DES," Comput. Fluids **78**, 10–23 (2013).
[8] E. Guilmineau, G. Deng, A. Leroyer, P. Queutey, M. Visonneau, and J. Wackers, "Assessment of hybrid RANS-LES formulations for flow simulation around the Ahmed body," Comput. Fluids **176**, 302–319 (2018).
[9] K. Liu, B. Zhang, Y. Zhang, and Y. Zhou, "Flow structure around a low-drag Ahmed body," J. Fluid Mech. **913**, A21 (2021).
[10] A. Rao, G. Minelli, B. Basara, and S. Krajnovic, "On the two flow states in the wake of a hatchback Ahmed body," J. Wind Eng. Ind. Aerodyn. **173**, 262–278 (2018).
[11] N. Ashton, A. West, S. Lardeau, and A. Revell, "Assessment of RANS and DES methods for realistic automotive models," Comput. Fluids **128**, 1–15 (2016).
[12] F. Delassaux, I. Mortazavi, E. Itam, V. Herbert, and C. Ribes, "Sensitivity analysis of hybrid methods for the flow around the Ahmed body with application to passive control with rounded edges," Comput. Fluids **214**, 104757 (2021).
[13] F. Sotiropoulos and X. Yang, "Immersed boundary methods for simulating fluid–structure interaction," Prog. Aerosp. Sci. **65**, 1–21 (2014).
[14] S.-G. Cai, A. Ouahsine, J. Favier, and Y. Hoarau, "Improved implicit immersed boundary method via operator splitting," in *Computational Methods for Solids and Fluids*, edited by A. Ibrahimbegovic (Springer Verlag, 2016), Vol. 41, Chap. 3, pp. 49–66.
[15] S.-G. Cai, A. Ouahsine, J. Favier, and Y. Hoarau, "Moving immersed boundary method," Int. J. Numer. Methods Fluids **85**, 288–323 (2017).
[16] S.-G. Cai, A. Ouahsine, J. Favier, and Y. Hoarau, "Implicit immersed boundary method for fluid–structure interaction," La Houille Blanche **103**, 33–36 (2017).
[17] S. Wilhelm, J. Jacob, and P. Sagaut, "An explicit power-law-based wall model for lattice Boltzmann method-Reynolds-averaged numerical simulations of the flow around airfoils," Phys. Fluids **30**, 065111 (2018).
[18] S.-G. Cai, J. Degrigny, J.-F. Boussuge, and P. Sagaut, "Coupling of turbulence wall models and immersed boundaries on Cartesian grids," J. Comput. Phys. **429**, 109995 (2021).
[19] J. Degrigny, S.-G. Cai, J.-F. Boussuge, and P. Sagaut, "Improved wall model treatment for aerodynamic flows in LBM," Comput. Fluids **227**, 105041 (2021).
[20] F. Capizzano, "Turbulent wall model for immersed boundary methods," AIAA J. **49**(11), 2367–2381 (2011).
[21] Y. Tamaki, M. Harada, and T. Imamura, "Near-wall modification of Spalart–Allmaras turbulence model for immersed boundary method," AIAA J. **55**(9), 3027–3039 (2017).
[22] H. Maeyama, T. Imamura, J. Osaka, and N. Kurimoto, "Turbulent channel flow simulations using the lattice Boltzmann method with near-wall modeling on a non-body-fitted Cartesian grid," Comput. Math. Appl. **93**, 20–31 (2021).
[23] S.-G. Cai, J. Jacob, and P. Sagaut, "Immersed boundary based near-wall modeling for large eddy simulation of turbulent wall-bounded flow," Comput. Fluids (submitted) (2022).
[24] J. Jacob, O. Malaspinas, and P. Sagaut, "A new hybrid recursive regularized Bhatnagar–Gross–Krook collision model for lattice Boltzmann method-based large eddy simulation," J. Turbul. **19**, 1051–1076 (2018).
[25] A. Vreman, "An eddy-viscosity subgrid-scale model for turbulent shear flow: Algebraic theory and applications," Phys. Fluids **16**, 3670–3681 (2004).
[26] A. Cahuzac, J. Boudet, P. Borgnat, and E. Lévêque, "Smoothing algorithms for mean-flow extraction in large-eddy simulation of complex turbulent flows," Phys. Fluids **22**, 125104 (2010).
[27] H. Xu and P. Sagaut, "Analysis of the absorbing layers for the weakly-compressible lattice Boltzmann methods," J. Comput. Phys. **245**, 14–42 (2013).
[28] J. Larsson, S. Kawai, J. Bodart, and I. Bermejo-Moreno, "Large eddy simulation with modeled wall-stress: Recent progress and future directions," Mech. Eng. Rev. **3**, 15-00418 (2016).
[29] S.-G. Cai and P. Sagaut, "Explicit wall models for large eddy simulation," Phys. Fluids **33**, 041703 (2021).
[30] S. Chen, Z. Xia, S. Pei, J. Wang, Y. Yang, Z. Xiao, and Y. Shi, "Reynolds-stress-constrained large-eddy simulation of wall-bounded turbulent flows," J. Fluids Mech. **703**, 1–28 (2012).

[31]A. Verma, N. Park, and K. Mahesh, "A hybrid subgrid-scale model constrained by Reynolds stress," Phys. Fluids **25**, 110805 (2013).
[32]L. Temmerman, M. A. Leschziner, C. P. Mellen, and J. Fröhlich, "Investigation of wall-function approximations and subgrid-scale models in large eddy simulation of separated flow in a channel with streamwise periodic constrictions," Int. J. Heat Fluid Flow **24**, 157–180 (2003).
[33]D. Monfort, S. Benhamadouche, and P. Sagaut, "Meshless approach for wall treatment in large-eddy simulation," Comput. Methods Appl. Mech. Eng. **199**, 881–889 (2010).
[34]H. Lienhart and S. Becker, "Flow and turbulence structure in the wake of a simplified car model," SAE Paper No. 2003-01-0656, 2003.
[35]See https://www.kbwiki.ercoftac.org/w/index.php/Description_AC1-05 for information about the case (accessed January 2, 2022).
[36]R. Howard and M. Pourquie, "Large eddy simulation of an Ahmed reference model," J. Turbul. **3**, N12 (2002).
[37]W. Meile, G. Brenn, A. Reppenhagen, B. Lechner, and A. Fuchs, "Experiments and numerical simulations on the aerodynamics of the Ahmed body," CFD Lett. **3**, 32–39 (2011).